Al/Fe isomorphic substitution versus Fe<inf>2</inf>O<inf>3</inf> clusters formation in Fe-doped aluminosilicate nanotubes (imogolite)

DOI:10.1007/s11051-015-3130-2

Shafia, Ehsan; Esposito, Serena; Manzoli, Maela; Chiesa, Mario; Tiberto, Paola; Barrera, Gabriele; Menard, Gabriel; Allia, Paolo; Freyria, Francesca S.; Garrone, Edoardo; Bonelli, Barbara. Al/Fe isomorphic substitution versus Fe2O3 clusters formation in Fe-doped aluminosilicate nanotubes (imogolite). JOURNAL OF NANOPARTICLE RESEARCH. 17 (8) pp: 1-14.
DOI: 10.1007/s11051-015-3130-2

“Magnetic properties of Fe-doped aluminosilicate nanotubes”

Ehsan Shafia,[1] *Serena Esposito,*[2] *Maela Manzoli,*[3] *Mario Chiesa,*[3] *Paola Tiberto,*[4] *Gabriele Barrera,*[3,4] *Gabriel Menard,*[5] *Paolo Allia,*[1,*] *Francesca S. Freyria,*[6] *Edoardo Garrone,*[1] *Barbara Bonelli*[1,*].

[1]*Department of Applied Science and Technology and INSTM Unit of Torino-Politecnico, Politecnico di Torino, Corso Duca degli Abruzzi 24, I-10129, Turin (Italy).*

[2] *Department of Civil and Mechanical Engineering, Università degli Studi di Cassino e del Lazio Meridionale, Via G. Di Biasio 43, 03043 Cassino (FR), Italy.*

[3]*Dipartimento di Chimica and Centro Interdipartimentale NIS, Università di Torino, Via Giuria 7, 10125, Turin, (Italy).*

[4]*Electromagnetism, I.N.Ri.M., Strada delle Cacce 91, 10135, Turin (Italy).*

[5]*Department of Chemistry and Chemical Biology, Harvard University, 12 Oxford St., Cambridge, MA, 02138, United States.*

[6]*Department of Chemistry, Massachusetts Institute of Technology, 77 Massachusetts Ave, 02139 Cambridge, (MA, USA)*

* Corresponding authors: Tel. +39 011 0904719 Fax. +39 011 0904624; *e-mail*: barbara.bonelli@polito.it (Prof. Barbara Bonelli); Tel. +39 011 0907336 Fax. +39 011 0904624; *e-mail*: paolo.allia@polito.it (Prof. Paolo Allia).

Abstract

Fe-doped aluminosilicate nanotubes with formula $(OH)_3Al_2$-xFexO$_3$SiOH were obtained with Fe content corresponding to either 0.7 or 1.4 % by weight. Fe was found to preferentially substitute Al when the NTs were obtained by direct synthesis, giving rise to high-spin Fe^{3+} sites, as detected by EPR, with Fe^{3+} ions isomorphically substituting for octahedral Al^{3+} ions located at the external surface of NTs. By post-synthesis loading, Fe preferentially forms Fe_2O_3 nanoclusters, due to the natural tendency of iron to form Fe-O-Fe bridges, as documented by both HRTEM and DR-UV-Vis analysis: some isomorphic substitution also takes place, as during direct synthesis.

The materials were also characterized from the magnetic point of view, which allows quantification of the amount of Fe^{3+} that isomorphically substitute for Al^{3+}, a piece of information not readily achievable by means of other experimental techniques.

Introduction

Imogolite (IMO) is a hydrated alumino-silicate with formula $(OH)_3Al_2O_3SiOH$ (Cradwick et al. 1972; Yoshinaga and Aomine 1962) either found in volcanic soils or prepared by sol-gel synthesis (Farmer et al. 1983; Farmer and Fraser 1978; Wada et al. 1979;). Bridged Al(OH)Al groups, with octahedrally coordinated (Oh) Al atoms, occur at NTs outer surface and non-interacting silanols (SiOH) at the inner surface (Scheme 1). The length of a single IMO NT varies between 400 nm and several microns, whereas the inner diameter is constant at 1.0 nm. The outer diameter is *ca.* 2.0 in natural IMO, whereas it varies around 2.5-2.7 nm in synthetic samples (Cradwick et al. 1972) due to the presence of different inter-tubes impurities.

IMO NTs arrange in bundles with nearly hexagonal packing. This structure gives rise to three kinds of pores (Ackerman et al. 1983; Wilson et al. 2002) shown in Scheme 2: (i) pores A are intra-tubes pores, 1.0 nm in diameter, lined by silanols, the related A surface being very hydrophilic and able to interact with probes like H_2O, NH_3 and CO (Bonelli et al. 2009; Bonelli et al. 2013); (ii) pores B, 0.3-0.4 nm wide, are those among three aligned NTs within a bundle, hardly accessible even to small molecules, like water (Ackerman et al. 1983; Wilson et al. 2002); (iii) pores C are slit mesopores among bundles, the surface of which may interact with larger molecules, like phenol (Bonelli et al. 2009) and 1,3,5-triethylbenzene (Bonelli et al. 2013).

The interest in IMO-related chemistry has spread recently, one reason being the possibility of changing the composition of both inner and outer surface of NTs. The former can be modified in several ways: (i) by substitution of Si atoms by Ge atoms, ither single or double walled NTs are given rise with formula $(OH)_3Al_2O_3Si_{1-x}Ge_xOH$ (Mukherjee et al. 2005; Thill et al. 2012); (ii) by grafting organic functionalities at the inner surface of IMO, $(OH)_3Al_2O_3SiO$-R NTs result, where R is the organic group (Kang et al. 2011); (iii) by properly choosing the Si precursor, hybrid NTs with formula $(OH)_3Al_2O_3Si$-R (R = $-CH_3$, $-(CH_2)_3-NH_2$) form by direct synthesis (Bottero et al. 2011; Kang et al. 2014).

The present work concerns yet another modification of the outer surface, the isomorphic substitution of Fe^{3+} for Oh Al,$^{3+}$ which the two available studies (Ookawa et al. 2006; Ookawa 2012) indicate to be possible up to a Fe content of 1.4 wt %. On the one hand, the presence of Fe^{3+} may impart the solid new chemical and solid-state properties; on the other hand, Fe^{3+}substitution for Al^{3+} is a very common natural process with all alumino-silicates.

Two samples were synthesized with 1.4 wt % Fe content, by adopting either direct (Fe-x-IMO) or post-synthesis (Fe-L-IMO) procedures differing, *inter alia*, in the silicon and aluminum precursors from the already reported method (Ookawa et al. 2006; Ookawa 2012). A third sample was obtained by direct synthesis, with an iron content corresponding to 0.7 % by weight. Morphological and textural properties of the three Fe-doped IMO, as measured by means of several techniques, are compared in the present paper to those of proper IMO. The properties induced by the presence of (different) Fe species are also studied by three different techniques: magnetic moment measurements, Mössbauer spectroscopy and EPR (Electron Paramagnetic Resonance).

Experimental

Materials

IMO was obtained as reported elsewhere (Bonelli et al. 2009).

Fe-x-IMO samples were obtained by direct synthesis as follows: in a glove box, a proper amount of $FeCl_3$*$6H_2O$ was added to 20 mM solution of $HClO_4$, then TEOS (tetraetoxysilicate) and Al-sec-butoxide were added, the pH of the resulting mixture being = 4.0. The aqueous mixture was stirred at room temperature for 18 h, diluted to 20 mM in Al, autoclaved at 373 K for 4 days, filtered, washed and dried overnight at 323 K in oven. A reddish-brown powder was obtained, the solution recovered by filtration being instead transparent.

Fe-L-IMO was prepared by contacting proper amounts of IMO and $FeCl_3$*$6H_2O$ in water (resulting pH = 4.0) for 24 h under stirring and finally adding NH4OH solution (33% by weight) to precipitate all Fe^{3+} as oxo/hydroxide. The solid was then filtered, washed and dried in oven at 323 K overnight. Chemical analysis of the supernatant solution did not detect the presence of residual iron with all the Fe-doped samples.

Methods

Electron micrographs were obtained on a high resolution transmission electron microscope (HRTEM, Jeol 3010-UHR) operating at 300 kV, equipped with a LaB_6 filament and with an Oxford Inca Energy TEM 300 EDS X-rays analyzer (Oxford Link) for atomic recognition. Digital micrographs were acquired by a (2k x 2k)-pixel Ultrascan 1000 CCD camera and processed by Gatan digital micrograph. Before HRTEM measurements, the powder samples were milled in an agate mortar and deposited on a copper grid covered with a lacey carbon film.

Powder X-Ray Diffraction (XRD) patterns were obtained on a X'Pert Phillips diffractometer operating with Cu Ka radiation (1.541874 Å) in the 2.5 – 18° 2θ range (step width = 0.02°, time per step: 2.00s).

To determine BET SSA (Brunauer-Emmett-Teller Specific Surface Area) and porous volume values reported in Table 1, N_2 isotherms were measured at 77 K on samples previously outgassed at 523 K, in order to remove water and other atmospheric contaminants, still preserving NT structure (MacKenzie et al. 1989; Zanzottera et al. 2012). NL-DFT (Non Local Density Functional Theory Method) was used to determine Pores Size Distributions (PSDs), by using a N_2-silica kernel for cylindrical pores.

Diffuse Reflectance (DR) UV-Vis spectra of samples outgassed at 523 K were measured on a Cary 5000 UV-Vis-NIR spectrophotometer (Varian instruments).

The zero-field ^{57}Fe Mössbauer spectra were measured with a constant acceleration spectrometer (SEE Co, Minneapolis, MN). The Fe-containing samples (*ca.* 50 mg) were prepared as Paratone-N mulls and frozen in liquid nitrogen prior to insertion into the spectrometer. Isomer shifts are quoted relative to Fe metal at 296 K. Data were acquired at 90 K and processed, simulated, and analyzed using an in-house package for IGOR Pro 6 (Wavemetrics, Lake Oswego, OR).

EPR spectra were recorded at 77 K on a Bruker EMX spectrometer operating at X-band frequency (9.78 GHz) and equipped with a cylindrical cavity operating at a 100 kHz field modulation. A modulation amplitude of 0.3 mT was used and the microwave power was adjusted to prevent saturation of the spin systems.

Room temperature magnetization curves were measured by means of an ultra-sensitive alternating-gradient field magnetometer (AGFM; sensitivity 1 $\times 10^{-8}$ emu) operating in the magnetic field range -18 kOe < H < 18 kOe and equipped with a sample-holder suitable for measurements on magnetically diluted systems such as the present IMO NTs.

Results and discussion

Textural properties of the studied samples

A thorough TEM characterization was carried out on all the samples. Figure 1 shows selected images collected on IMO, at different magnifications, concerning, respectively, a whole particle (section a), a bundle with parallel NTs (section b), and a detail of a bundle termination, showing a hexagonal array of NTs (section c).

The morphological features of bare IMO were maintained after Fe-doping, independently of both Fe amount and synthesis procedure (Fig. 2a, 2d, 2f and 2h). In addition, Fe is homogeneously distributed, as demonstrated by the EDS maps of the Fe-doped samples (Fig. 2c, 2g, 2i), pointing out the effectiveness of both synthesis procedures. Some Fe-containing nanoclusters at the outer surface of NTs were observed in Fe-L-IMO sample (arrows in Fig. 2h). The size of Fe-containing nanoclusters was evaluated by considering electron micrographs acquired at 50,000 magnification, where nanoclusters, well contrasted with respect to the IMO material, were clearly seen. The particle size distribution in Fig. 2h was obtained by considering 450 particles: the average particle diameter ($d_m \approx 4.4$ nm) was calculated as $d_m = \Sigma d_i n_i / \Sigma n_i$, where n_i is the number of particles of diameter d_i.

Figure 3 reports XRD patterns of IMO, Fe-0.025-IMO, Fe-0.05-IMO, and Fe-L-IMO, all corresponding to hexagonal packing of NTs clearly visible in Fig. 1. The d_{100} diffraction is at $2\theta = 3.88°$ with both IMO and Fe-L-IMO (vertical bar), and at slightly higher 2θ values with both Fe-0.025-IMO ($2\theta = 4.03°$) and Fe-0.05-IMO ($2\theta = 4.06°$). The cell parameter *a* (*i.e.* the distance between two aligned NTs, Scheme 2) is 2.62 nm with both IMO and Fe-L-IMO (Table 1), and 2.51 nm with both Fe-x-IMO samples.

Such a difference is not related to the occurrence of Al^{3+}/Fe^{3+} isomorphic substitution that is expected to increase the *a* value: magnetic measurements, reported below, showed indeed that isolated Oh Fe^{3+} species are in high spin configuration, to which a Shannon radius of 0.645 Å corresponds, definitely larger than that of Oh Al^{3+} (0.535 Å).

N_2 adsorption isotherms in Figure 4a show the (expected) features for microporous systems with some mesoporosity (Table 1). Note that Fe-L-IMO has a larger mesopores volume, because the loading procedure mainly affects the C surface. In agreement with the hypothesis of the Al^{3+}/Fe^{3+} isomorphic substitution, PSDs curves in section *b* of the Figure show a slight increase in diameter in the sequence IMO = Fe-L-IMO < Fe-0.025-IMO < Fe-0.05-IMO: absolute values are not entirely worth of trust, being lower than 1.0 nm, but the trend is most probably reliable. Further support comes from the HRTEM pictures: internal pores diameter, carefully measured on several images on both IMO and Fe-x-IMO samples, showed an increase in the series IMO (1.05 nm) < Fe-0.025-IMO (1.29 nm) < Fe-0.05-IMO (1.34 nm) (Figures 1c, 2b and 2e). The smaller *a* value for Fe-containing samples, as opposed to the probably larger internal diameter, is most likely due to the anions in the synthesis bath, not entering though the IMO formula, but joining together adjacent NTs. In natural samples, the *a* value may vary between 2.0 and 2.7 nm, without any change in inner diameter, because of the different impurities possibly present within inter-nanotubes spaces. With IMO, previous work (Zanzottera et al. 2012) has indeed shown the occlusion of some perchlorate anions coming from the synthesis batch, because the release of molecular oxygen at high temperature was observed by TG-mass analysis (Zanzottera et al. 2012). During the synthesis of Fe-x-IMO, chloride ions likely replace (larger) perchlorate anions, so decreasing the final *a* value. Indeed, thermal treatment of both Fe-x-IMO samples did not show any release of oxygen, as measured by TG-Mass analysis (not reported).

State of iron species as studied by Mössbauer, DR-UV-Vis and EPR spectroscopies

The zero-field ^{57}Fe Mössbauer spectra of Fe-containing IMO are shown in Figure 5, all featuring very similar single quadrupole doublets. Both Fe-L-IMO and Fe-0.025-IMO samples have identical isomer shift (δ) and quadrupole splitting ($|\Delta E_Q|$) values (δ, $|\Delta E_Q|$ (mm/s): 0.46, *0.73*, Figs. 5a and 5c, respectively), whereas Fe-0.05-IMO has a slightly larger quadrupole splitting value (δ, $|\Delta E_Q|$ (mm/s): 0.46, *0.80*, Fig. 5b). These data are consistent in all cases with Fe centers in the 3+ oxidation state (Fallet et al. 2003; Lopez et al. 2002). As expected, with IMO no Fe centers were detected by ^{57}Fe Mössbauer spectroscopy (spectrum not reported).

DR UV-Vis spectra of dehydrated samples are reported in Figure 6: IMO has, as expected, a negligible absorption in the UV-Vis region (curve 1); both Fe-x-IMO samples (curves 2 and 3) strongly absorb at 270 nm, and show a minor absorption band at 480 nm: according to the literature, the former signal is due to charge-transfer transitions (CT) from O^{2-} to isolated Oh Fe^{3+} ions, the latter to *d-d* transitions of Fe^{3+} in Fe_2O_3 nanoclusters (Wang et al. 2002). Fe-L-IMO spectrum (curve 4) is shifted to higher wavelengths and strongly absorbs in the region of *d-d* transitions, because of the preferential formation of Fe_2O_3 nanoclusters (Wang et al. 2002) by post-synthesis method, although the sample also absorbs at 270 nm. With the Fe-containing samples, both isolated Oh Fe^{3+} species and aggregated Fe-O-Fe groups are obtained, the latter more abundant with Fe-L-IMO. The presence of isolated Oh Fe^{3+} sites in Fe-L-IMO indicates that ionic exchange also occurred between structural Al^{3+} and Fe^{3+} ions in water:

$$[Al(OH)^{+}Al]_{(s)} + Fe(H_2O)_6^{3+} \rightarrow [Fe(OH)^{+}Al]_{(s)} + Al(H_2O)_6^{3+} \qquad (1)$$

On the other hand, the occurrence of some Fe_2O_3 nanoclusters in Fe-x-IMO indicates that the actual isomorphic substitution of Fe for Al in the IMO structure is probably lower than that corresponding to 1.4% by weight.

To elicit information about the nature of different Fe^{3+} species, EPR spectroscopy was used to study both Fe-0.025-IMO and Fe-L-IMO samples. Fig. 7a shows EPR spectra of fresh samples, which are dominated by an absorption feature at g_{eff}=4.3 and two broad lines, largely superimposed, at $g_{eff} \cong 2.0$ and 2.3. In aluminum-silicates, Fe^{3+} is usually present in high spin ferric state (S=5/2), consistently with the weak ligand field provided by possible ligands (water, hydroxide or oxide ions). Under those circumstances, the X-band EPR spectrum usually consists of a prominent peak at $g_{eff} = 4.3$ and possible other broader peaks down to $g_{eff} \cong 9$. The g_{eff}=4.3 line observed in Fig. 7a is assigned to the presence of isolated Fe^{3+} ions in high spin state, likely corresponding to species absorbing at 270 nm in the DR-UV-Vis spectra. The relative intensity of the g_{eff}=4.3 line is slightly higher with Fe-0.025-IMO, the sample at lower Fe loading, in agreement with other authors (Goldfarb et al. 1994). The $g_{eff} \cong 2.0$ and 2.3 lines are usually associated to iron oxide clusters and/or particles where Fe^{3+} ions strongly interact with each other (Goldfarb et al. 1994; Bordiga et al 1996; Ferretti et al. 2004). Any evaluation of the relative spin concentration of isolated and clustered Fe^{3+} species is hampered, in this case, due to the high anisotropy in the transition probabilities of Fe^{3+} high spin states.

Upon dehydration of the samples at 473 K (Fig. 7b), the feature at $g_{eff}=2.0$ strongly reduces in intensity, while the signal at $g_{eff}=2.3$ increases in particular with Fe-0.025-IMO. A similar behaviour, already reported in iron-loaded zeotype materials, was attributed to the formation of “aggregated” Fe^{3+} species ~~within the porous structure~~ brought about by de-hydration (Berlier et al. 2002; Umamaheswari et al. 2006). Assuming the $g_{eff}=4.3$ signal to be a marker of structural Fe^{3+}, its intensity remains almost constant in the two samples despite the different iron loading, indicating that the corresponding sites are rather stable.

In order to verify the chemical reactivity of Fe^{3+} species and possible presence of reduced Fe^{2+} species, 10 mbar of NO were dosed at room temperature on the two dehydrated samples (Figure 7c): during thermal treatment, reduction from (reactive) Fe^{3+} species to EPR silent Fe^{2+} species was indeed reported for other materials (Joyner and Stockenhuber 1999; Fisicaro et al. 2003). Such Fe^{2+} species readily react with NO to form Fe^{2+}–NO complexes, with total spin $S=3/2$, that are characterized by distinct EPR signals, dominated by a feature at $g_{eff}=4.0$

(Umamaheswari et al. 2006). In the present case, no EPR signal typical for Fe^{2+}*–NO complexes was observed in Fig 7c, indicating that no reduction of* Fe^{3+} *occurs under the applied treatment, in agreement with the assumption of the framework nature of these sites.*

Formation of Fe^{3+}*-NO adducts is expected to lead to integer spin states that are not observable at the operational frequency used in this study (9.5 GHz) (Pilbrow 1990). Comparison of the* Fe^{3+} *signal prior and after NO adsorption (Fig 7b and 7c, respectively), however, indicates that no reduction in the EPR signal intensity occurs, suggesting that no such complexes are formed. This may be explained by considering that the EPR active* Fe^{3+} *species are co-ordinatively saturated and not capable to coordinate the NO molecule. Evidence for NO physisorption at strongly polarizing cationic sites is instead provided by a small signal (asterisk in Fig. 7c), typical for NO molecules adsorbed on* Al^{3+} *sites in aluminosilicate zeotype materials (Pöpple et al. 2004; Lunsford 1968).*

Magnetic data

Isothermal magnetization curves of the samples measured at room temperature are reported in Figure 8; the magnetic response of the sample holder has been measured and subtracted from the data in order to get rid of spurious magnetic effects from the measuring setup. IMO exhibits a pure diamagnetic behaviour;

instead, Fe-x-IMO and Fe-L-IMO samples display a dominant paramagnetic response.

In order to single out the magnetic contribution from Fe ions, the magnetization of IMO (expressed in emu per gram of material) has been subtracted from the Fe-doped samples; the resulting M(H) curves are shown in Figure 9 and confirm that Fe-0.025-IMO is perfectly paramagnetic. Amore complex behaviour, where a sigmoidal, anhysteretic magnetic signal is superimposed to an underlying paramagnetic response, is observed in both Fe-0.05-IMO and Fe-L-IMO, the signal from Fe-0.05-IMO being much weaker (see inset of Figure 9). The sigmoidal curves have been obtained by subtracting the paramagnetic signal (estimated by fitting the high-field slope of the M(H) curves, and are reported in Figure 10.

The theoretical number N of Fe ions per gram of substance in Fe-doped samples ($N = 7.55 \times 10^{19}$ ions/g for Fe-0.025-IMO and $N = 1.51 \times 10^{20}$ ions/g for Fe-0.05-IMO and Fe-L-IMO) has been evaluated starting from the nominal compositions. According to the simplest model, the magnetic susceptibility of a Van Vleck's paramagnet (Coey 2009) is $\chi_{para} = \frac{N g_J^2 \mu_B^2 S(S+1)}{3 k_B T}$, where T is the measurement temperature, μ_B is the Bohr magneton, k_B the Boltzmann's constant. For isolated Fe^{3+} ions, the ionic Landé factor is $g_J = 2$ (please note that the g_J factor used in the analysis of magnetic susceptibility measurements is different from the electronic g_{eff} factor as determined by EPR measurements) and J=S=5/2 according to the Hund's rules. Using T = 293 K, the value for the magnetic susceptibility is predicted to be $\chi_{para} = 1.87 \times 10^{-6}$ emu $g^{-1}Oe^{-1}$ in Fe-0.025-IMO and $\chi_{para} = 3.75 \times 10^{-6}$ emu $g^{-1}Oe^{-1}$ in both Fe-0.05-IMO and Fe-L-IMO. The straight lines $M_{theo}(H)$ obtained using the two theoretical values of χ_{para} are reported in Figure 9 (open and full symbols, respectively).

A notable agreement between the theoretical prediction and the experimental curve is found for Fe-0.025-IMO. The slight difference in slope can be ascribed to the intrinsic limit of the simple model used here. Magnetic susceptibility measurements therefore indicate that in this material virtually all magnetic species introduced in IMO by direct synthesis appear in the form of substitutional, basically non-interacting high-spin Fe^{3+} ions, perfectly in line with the results of DR-UV-Vis spectra and EPR measurements.

In both samples containing a larger nominal amount of Fe ions the prediction for the Van Vleck's paramagnetic susceptibility leads to a theoretical line with a definitely higher slope than the one actually measured.

In both Fe-0.05-IMO and Fe-L-IMO, the sigmoidal curves obtained by subtraction (Figure 10) reveal a phase comprised of non-isolated Fe^{3+} ions and points to the presence of magnetic nanoparticles, in agreement with the results of TEM analysis and resonance/spectroscopy methods, both indicating the existence of Fe_2O_3 nanoclusters. The magnetic response of these small nanoparticles/nanoclusters is compatible with both hematite (α-Fe_2O_3) and maghemite (γ-Fe_2O_3) structure. Hematite (α-Fe_2O_3) exhibits an antiferromagnetic behaviour below the Morin temperature (Chikazumi 1997) and becomes a weak ferromagnet above; the transition occurs well below room temperature in bulk hematite and at even lower temperatures in hematite nanoparticles (Eid et al. 2011); as a consequence, hematite nanoparticles possibly present in these samples should exhibit a weak ferromagnetic signal at room temperature; a closely similar signal should arise from maghemite nanoparticles too because γ-Fe_2O_3 is a ferrimagnetic compound (Chikazumi 1997).

However, the nanoparticles observed by TEM in the present samples are small ($d_m \cong 4.4$ nm) and characterized by a very high surface-to-volume ratio, so that it can be presumed that the actual distribution of magnetic moment directions in each nanoparticle is dominated by strong, site-dependent surface anisotropy (Zysler 2005), basically resulting in a highly disordered, spin-glass-like arrangement of magnetic moments (Kodama 1996). In this case, the magnetic moments are extremely correlated and are predicted to be quite insensitive to an applied magnetic field having maximum amplitude comparable to the one used in the present measurements. This picture would actually apply to both hematite and maghemite nanoparticles.

The relative amount of Fe ions in the two main phases evidenced by susceptibility measurements (substitutional Fe^{3+} ions and α/γ-Fe_2O_3 nanoclusters) can be estimated by comparing the actual slopes of the M(H) curves with the theoretical predictions for the nominal concentrations. The experimental number of Fe^{3+} ions in the pure paramagnetic phase turns out to be $N_{exp} = 9.35 \times 10^{19}$ ions/g in Fe-0.050-IMO and $N_{exp} = 9.46 \times 10^{19}$ ions/g in Fe-L-IMO. These values can be easily transformed into percentages, shown along with the nominal Fe concentrations in Figure 11. In Fe-L-IMO, the estimated number of Fe ions in the Fe_2O_3 nanoclusters turns out to be $(N\text{-}N_{exp}) = 5.64 \times 10^{19}$ ions/g (per gram of material), corresponding to a fraction f = 0.374 of the total Fe mass introduced in the material; therefore, the mass of Fe in nanoclusters is 5.23×10^{-3} g (per gram of material). A calculation performed on Fe-0.05-IMO brings about a very similar value (5.33×10^{-3} g) for the mass of Fe in nanoclusters (per gram of material).

The magnetization curves shown in Figure 10 can therefore be expressed per gram of Fe in nanoclusters (emu/g[Fe]; right-side axis). It may be noted that the maximum magnetization from Fe_2O_3 nanoclusters in both Fe-0.05-IMO and Fe-L-IMO (corresponding to perfect alignment of all spins on the magnetic sites) is estimated to be $M_{max} = (N\text{-}N_{exp})\, g_J\, [S(S+1)]^{1/2}\, \mu_B \cong 3.2$ emu/g[Fe] and 3.1 emu/g[Fe] respectively, i.e., almost more than twice the high-field value of M(H) we measure in Fe-L-IMO and about 8 times higher in Fe-0.05-IMO (see Figure 10). This result can be explained by considering that in the explored interval of magnetic field values the magnetic moments of nanoclusters are most effectively pinned by surface anisotropy and do not substantially contribute in the M(H) curve. The smaller sigmoidal signal observed in Fe-0.05-IMO could indicate a more efficient anisotropy pinning of magnetic moments and therefore a smaller average size of the Fe_2O_3 nanoclusters.

Conclusion

Experimental evidence is provided of the fact that Al^{3+}/Fe^{3+} isomorphic substitution is the major process occurring in Fe-doped IMO NTs produced by direct synthesis, although some isolated Oh Fe^{3+} ions also occur when the loading procedure is adopted. In the latter case, however, Fe_2O_3 nanoclusters formation mainly occurs at NTs outer surface.

Room-temperature magnetic susceptibility measurements indicate that not-loaded IMO NTs have a diamagnetic response as expected, whereas all loaded samples display a dominant paramagnetic behavior. In Fe-0.025-IMO the agreement between theoretical prediction and experimental data for the χ_{para} indicates that the paramagnetic signal entirely comes from isolated Fe^{3+} ions; in both Fe-0.05-IMO and Fe-L-IMO samples these measurements point to a lower-than-expected content of isolated Fe^{3+} ions, in agreement with the evidence from spectroscopy/resonance measurements indicating the presence of Fe_2O_3 nanoparticles; the magnetic moments in these nanoparticles are presumed to be highly disordered because of the pinning effect of a strong, random surface anisotropy; the sigmoidal magnetic signal basically arises from partial field-induced unpinning of a fraction of moments.

Captions to Figures

Figure 1. TEM images of an IMO bundle (a), formed by parallel NTs (b) that are organized into a hexagonal array (c). Instrumental magnification: 10000X in section a; 50000X in section b.

Figure 2. TEM images of Fe-0.025-IMO, Fe-0.05-IMO and Fe-L-IMO formed by parallel NTs (sections a, d and h, respectively) that are organized into a hexagonal array (zoom of section a, sections f and h). Sections b and e: Fe-0.025-IMO and Fe-0.05-IMO pore size distributions, respectively. Sections c, g and i: Fe-0.025-IMO, Fe-0.05-IMO and Fe-L-IMO bundles and corresponding EDS maps allowing the speciation of Si, Al, Fe and O elements. Instrumental magnifications: 10000X (section a), 40000X (section g) and 50000X (all the other sections).

Figure 3. Low angles XRD patterns of the following powder samples: IMO (1), Fe-L-IMO (2), Fe-0.025-IMO (3) and Fe-0.05-IMO (4).

Figure 4. Section a: N_2 sorption isotherms at 77 K of IMO (squares), Fe-L-IMO (circles), Fe-0.025-IMO (stars) and Fe-0.05-IMO (triangles) samples dehydrated at 523 K. Full and hollow symbols refer to adsorption and desorption branches, respectively. Section b: Pore size distributions of IMO (squares), Fe-L-IMO (circles), Fe-0.025-IMO (stars) and Fe-0.05-IMO (triangles) as obtained by applying the NL-DFT method.

Figure 5. Zero-field ^{57}Fe Mössbauer spectra at 90 K. Solid red line represents the fit to the data and yields the following parameters: a) for Fe-L-IMO, δ = 0.46 mm/s; $|\Delta E_Q|$ = 0.73 mm/s; b) for Fe0.05-IMO, δ = 0.46 mm/s; $|\Delta E_Q|$ = 0.80 mm/s and c) for sample Fe0.025-IMO, δ = 0.46 mm/s; $|\Delta E_Q|$ = 0.73 mm/s.

Figure 6. DR UV-Vis spectra of IMO (1), Fe-0.025-IMO (2), Fe-0.05-IMO (3) and Fe-L-IMO (4).

Figure 7. X-band EPR spectra of Fe-0.025-IMO (red curves) and Fe-L-IMO (blue curves): (a) fresh samples, (b) samples dehydrated for 1h at 473 K and (c) NO-loaded samples (10 mbar). All spectra were recorded at 77 K.

Figure 8. Room-temperature magnetization curves of IMO and Fe-doped IMO NTs after subtraction of the magnetic response of the experimental setup.

Figure 9. The same as in Figure 8 for Fe-doped IMO NTs after subtraction of the diamagnetic response from IMO NTs. Inset: magnified low-field curves of Fe-0.05-IMO and Fe-L-IMO samples.

Figure 10. Magnetic contribution from the surface of hematite nanoclusters in Fe-0.05-IMO and Fe-L-IMO. Left-side vertical scale: magnetization per gram of material; right-side vertical scale: magnetization per gram of Fe contained in the hematite nanoclusters

Figure 11. Iron content (expressed in wt% of the samples) in the form of isolated Fe^{3+} ions and hematite nanoclusters for all examined samples. The nominal Fe content is shown for comparison.

References

Ackerman W C, Smith D M, Huling J C, Kim Y, Bailey J K, Brinker C J (1993) Gas/Vapor Adsorption in Imogolite: A Microporous Tubular Aluminosilicate. Langmuir 9: 1051-1057.

Berlier G, Spoto G, Bordiga S, Ricchiardi G, Fisicaro P, Zecchina A, Rossetti I, Selli E, Forni L, Giamello E, Lamberti C (2002) Evolution of Extraframework Iron Species in Fe Silicalite: 1. Effect of Fe Content, Activation Temperature, and Interaction with Redox Agents. J Catal 208: 64-82.

Bonelli B, Armandi M, Garrone E (2013) Surface properties of alumino-silicate single-walled nanotubes of the imogolite type. Phys Chem Chem Phys 15: 13381-13390.

Bonelli B, Bottero I, Ballarini N, Passeri S, Cavani F, Garrone E (2009) IR spectroscopic and catalytic characterization of the acidity of imogolite-based systems. J Catal 264: 15–30.

Bordiga S, Buzzoni R, Geobaldo F, Lamberti C, Giamello E, Zecchina A, Leofanti G, Petrini G, Tozzola G, Vlaic G (1996) Structure and reactivity of framework and extra- framework ieon in Fe-silicalite as investigated by spectroscopic and physicochemical methods. J Catal 158: 486-501.

Bottero I, Bonelli B, Ashbrook S, Wright P, Zhou W, Tagliabue M, Armandi M, Garrone E (2011) Synthesis and characterization of hybrid organic/inorganic nanotubes of the imogolite type and their behaviour towards methane adsorption. Phys Chem Chem Phys 13: 744 -750.

Chikazumi S (1997) Physics of Ferromagnetism 1997 edition, Oxford University Press, Oxford. ISBN 0-19-851776-9.

Coey J M D (2009) Magnetism and Magnetic Material, Cambridge University Press, Cambridge. ISBN 9780521816144

Cradwick P D G, Farmer V C, Russell J D, Wada K, Yoshinaga N (1972) Imogolite, a Hydrated Aluminium Silicate of Tubular Structure. Nature Phys Sci 240: 187-189.

Eid C, Luneau D, Salles V, Asmar R, Monteil Y, Khoury A, Brioude A (2011) Magnetic properties of hematite nanotubes elaborated by electrospinning process. J Phys Chem C 115: 17643-17646.

Fallet M, Gschwind R, Bauer P (2003) Oxidation States of Iron in Doped TiO_2-SiO_2 Sol-Gel Powders: A ^{57}Fe Mössbauer Study. J Sol-Gel Sci Techn 27:167-173.

Farmer V C, Adams M J, Fraser A R, Palmieri F (1983) Clay Miner 18: 459-472.

Farmer VC, Fraser A R (1978) Synthetic Imogolite: a tubular hydroxyaluminium silicate. Proceedings of the International Clay Conference, Elsevier, Amsterdam 547-554.

Ferretti A M, Barra A L, Forni L, Oliva C, Schweiger A, Ponti A (2004) Electron Paramagnetic Resonance Spectroscopy of Iron(III)-Doped MFI Zeolite. 1. Multi-Frequency CW-EPR. J Phys Chem B 108: 1999-2005.

Fisicaro P, Giamello E, Berlier G, Lamberti C (2003) Paramagnetic nitrosyliron adducts in pentasilic zeolites: an EPR study. Res Chem Intermed 29: 805-816.

Goldfarb D, Bernardo M, Stoheimer K G, Vaughan D E W, Tomann H (1994) Characterization of Iron in Zeolites by X-band and Q-Band ESR, Pulsed ESR, and UV-Visible Spectroscopies. J Am Chem Soc 116: 6344-6353.

Joyner R W, Stockenhuber M (1999) Preparation, Characterization, and Performance of Fe−ZSM-5 Catalysts. J Phys Chem B 103:5963-5976.

Kang D-Y, Brunelli N A, Yucelen G I, Venkatasubramanian A, Zang J, Leisen J, Hesketh P J, Jones C W, Nair S (2014) Direct synthesis of aminoaluminosilicate nanotubes with enhanced molecular adsorption selectivity. Nature Commun: 3342.

Kang D-Y, Zang J, Jones C W, Nair S (2011) Single-Walled Aluminosilicate Nanotubes with Organic-Modified Interiors. J Phys Chem C 115: 7676-7685.

Kodama R H, Berkowitz A E, McNiff E J, Foner S (1996) Surface Spin Disorder in $NiFe_2O_4$ Nanoparticles. Phys Rev Lett 77: 394-397

Lopez T, Moreno J A, Gomez R, Bokhimi X, Wang J A, Yee-Madeira H, Pecchi G, Reyes P (2002) Characterization of iron-doped titania sol–gel materials. J Mater Chem 12: 714-718.

Lunsford J H (1968) Surface interactions of NaY and decationated Y zeolites with nitric oxide as determined by electron paramagnetic resonance spectroscopy. J Phys Chem 72: 4163-4168.

MacKenzie K J, Bowden M E, Brown J W M, Meinhold R H (1989) Structure and Thermal Transformations of Imogolite Studied by ^{29}Si and ^{27}Al High-Resolution Solid-State Nuclear Magnetic Resonance. Clay Clay Miner 37: 317-324.

Mukherjee S, Bartlow V M, Nair S (2005) Phenomenology of the growth of single-walled aluminosilicate and aluminogermanate nanotubes of precise dimensions. Chem Mater 17: 4900-4909.

Ookawa M (2012) Synthesis and characterization of Fe-Imogolite as an oxidation catalyst. In Clay Minerals in Nature - Their Characterization, Modification and Application, InTech. 239-257. ISBN 978-953-51-0738-5

Ookawa M, Inoue Y, Watanabe M, Suzuki M, Yamaguchi T (2006) Synthesis and Characterization of Fe Containing Imogolite. Clay Sci 12: 280-284.

Pilbrow J R (1990) Transition Ion Electron Paramagnetic Resonance, Clarendon Press, Oxford. ISBN: 0-198-55214-9

Pöpple A, Gutjahr M, Rudolf T (2004) in Molecules in Interaction with Surfaces and Interfaces, Lect. Notes Phys. 634 pag. 185, Springer, Berlin. ISBN 978-3-540-40024-0.

Thill A, Maillet P, Guiose B, Spalla O, Belloni L, Chaurand P, Auffan M, Olivi L, Rose J (2012) Physico-chemical Control over the Single- or Double-Wall Structure of Aluminogermanate Imogolite-like Nanotubes. J Am Chem Soc 134: 3780-3786.

Umamaheswari V, Böhlmann W, Pöppl A, Vinu A, Hartmann M (2006) Spectroscopic characterization of iron-containing MCM-58. Micropor Mesopor Mat 89: 47–57

Wada S I, Eto A, Wada K (1979) Synthetic Allophane and Imogolite. J. Soi. Sci: 347-355.

Wang Y, Zhang Q H, Shishido T, Takehira K (2002) Characterization of Iron-Containing MCM-41 and Its Catalytic Properties in Epoxidation of Styrene with Hydrogen Peroxide. J Catal 209: 186-196.

Wilson M A, Lee G S H, Taylor R C (2002) Benzene displacement on imogolite. Clays Clay Miner 50: 348-351.

Yoshinaga N, Aomine A (1962) Imogolite in some Ando Soils. Soil Sci Plant Nutr 8: 22-29.

Zanzottera C, Vicente A, Armandi M, Fernandez C, Garrone E, Bonelli B (2012) Thermal Collapse of Single-Walled Alumino-Silicate Nanotubes: Transformation Mechanisms and Morphology of the Resulting Lamellar Phases. J Phys Chem C 116: 23577–23584.

Zysler R D, De Biasi E, Ramos C A, Fiorani D, Romero H (2005) Surface and Interparticle Effects in Amorphous Magnetic Nanoparticles in Surface Effects in Magnetic Nanoparticles edited by D. Fiorani, Springer Science+Business Media, New York USA pp. 239-261.

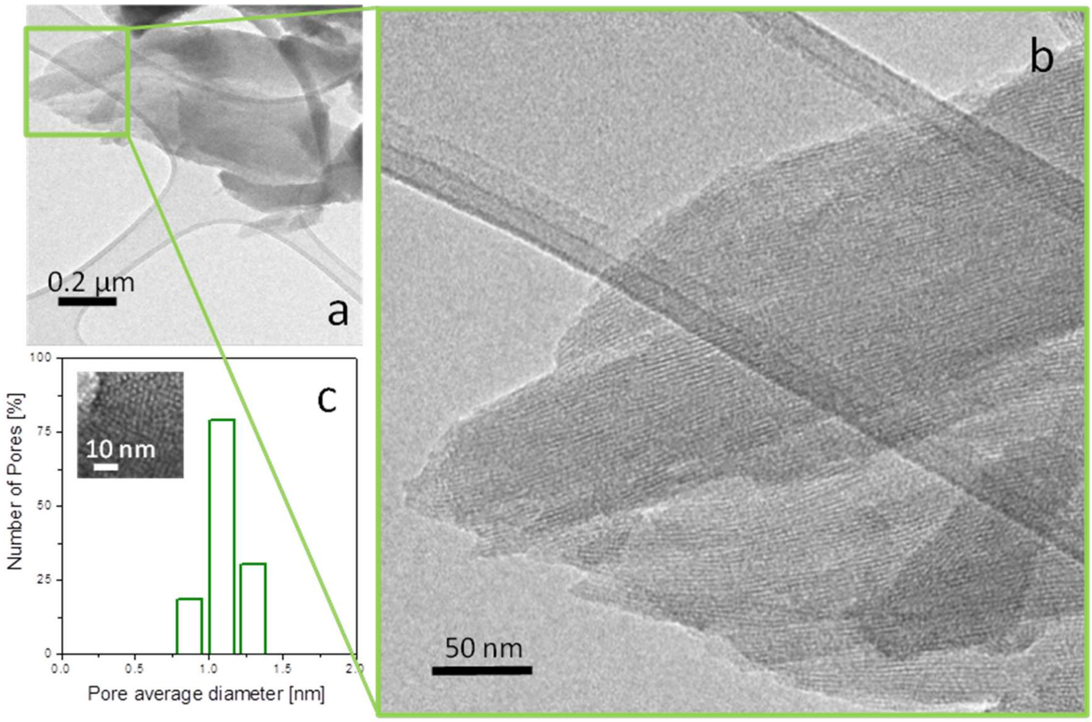

Figure 1. E. Shafia et al.

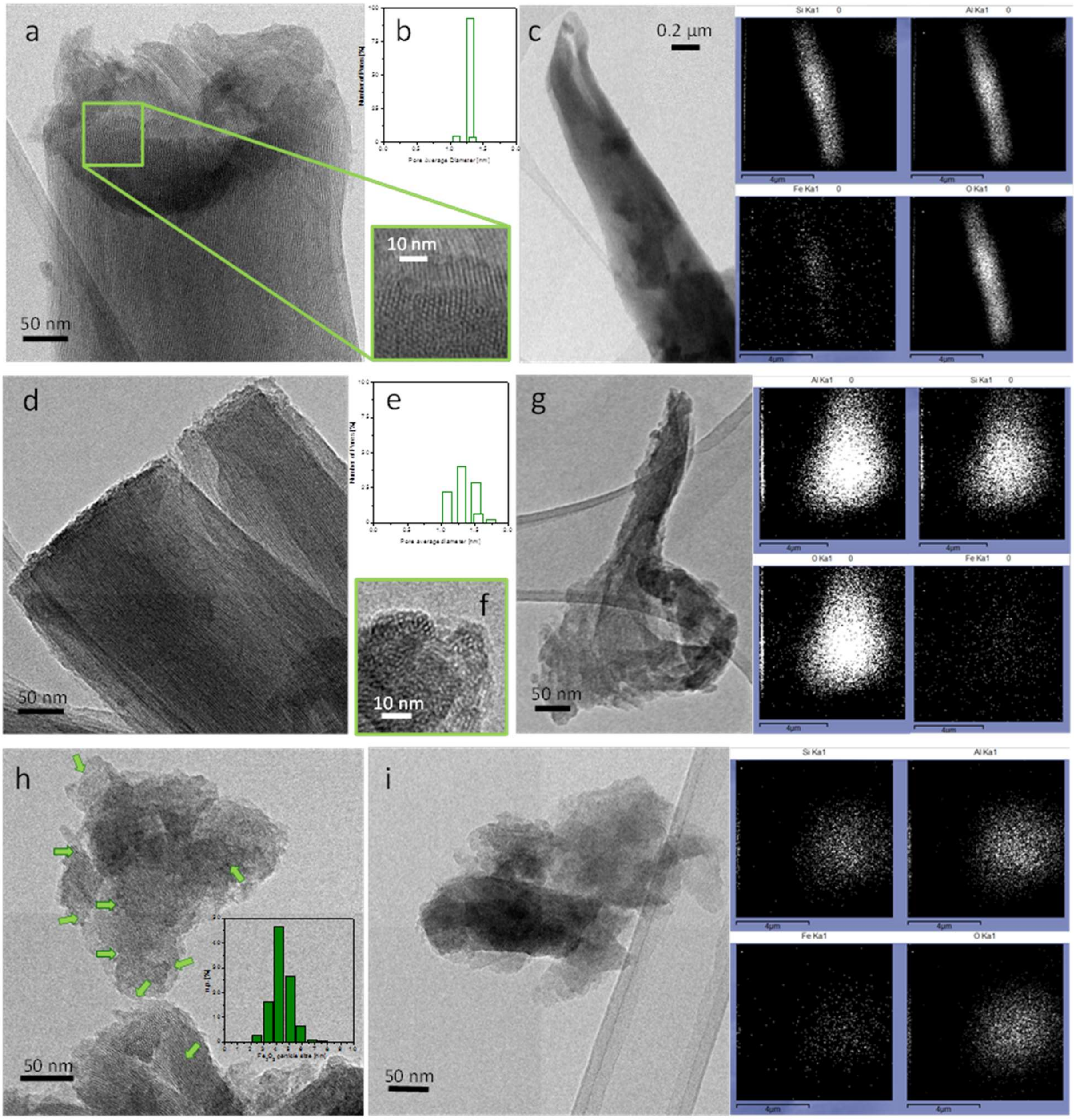

Figure 2. E. Shafia et al.

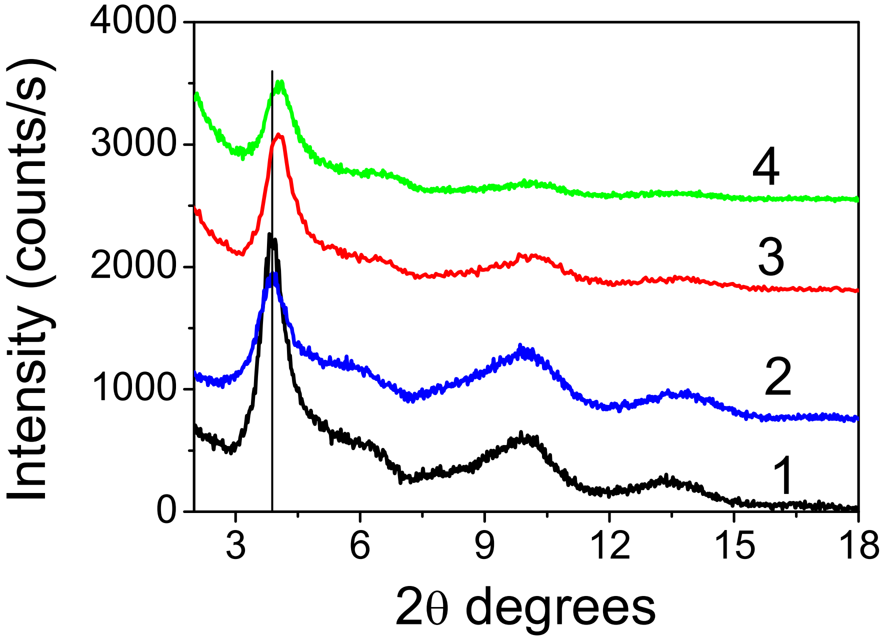

Figure 3. E. Shafia et al.

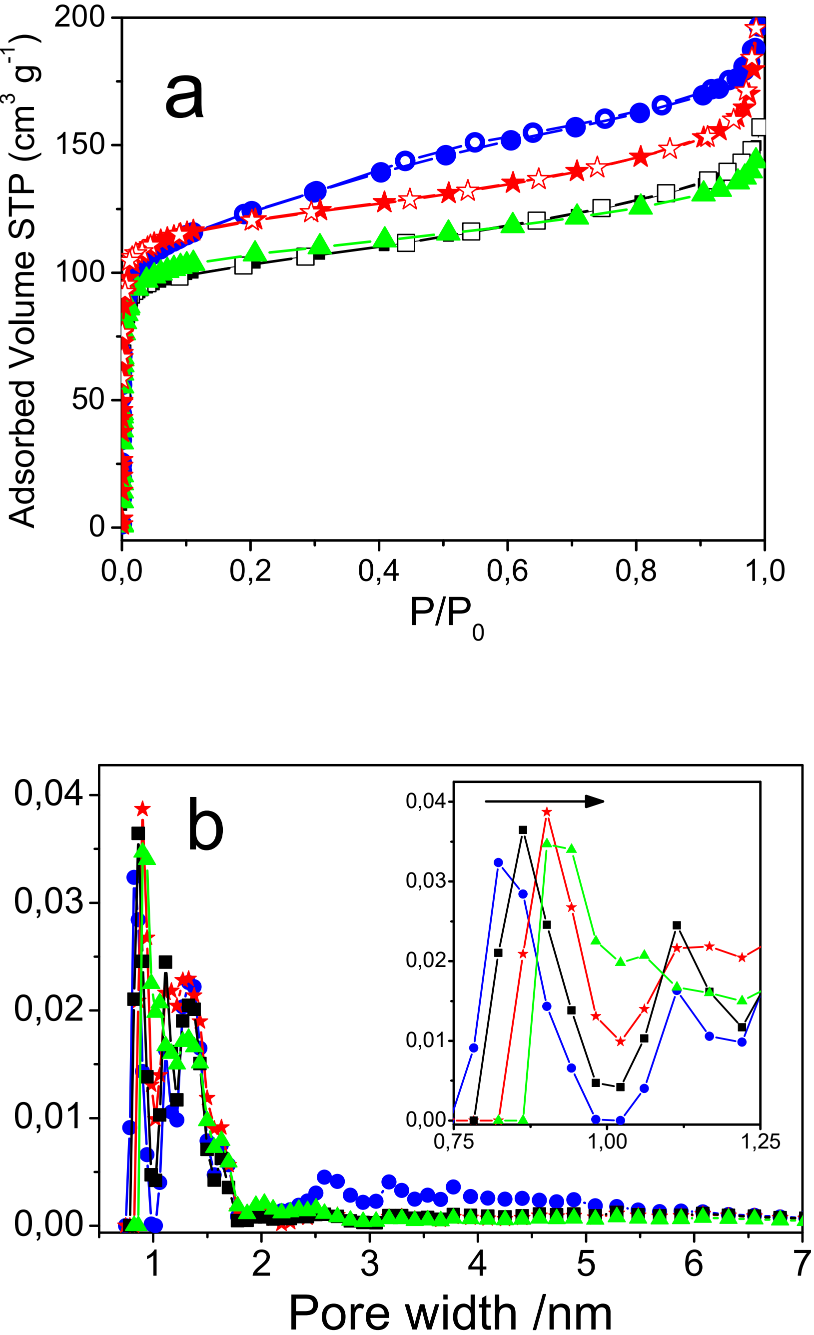

Figure 4. E. Shafia et al.

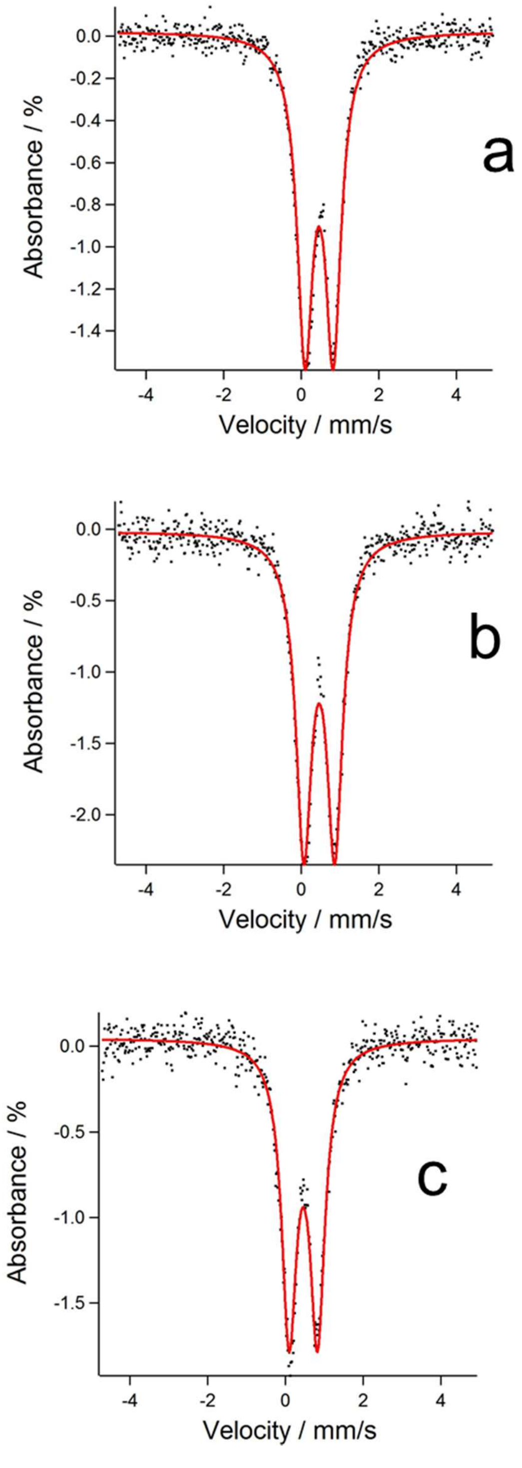

Figure 5. E. Shafia et al.

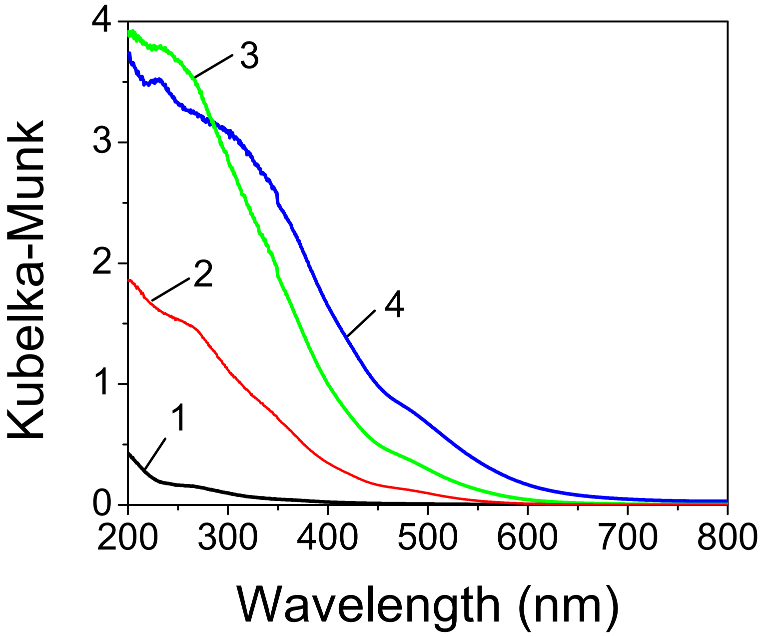

Figure 6. E. Shafia et al.

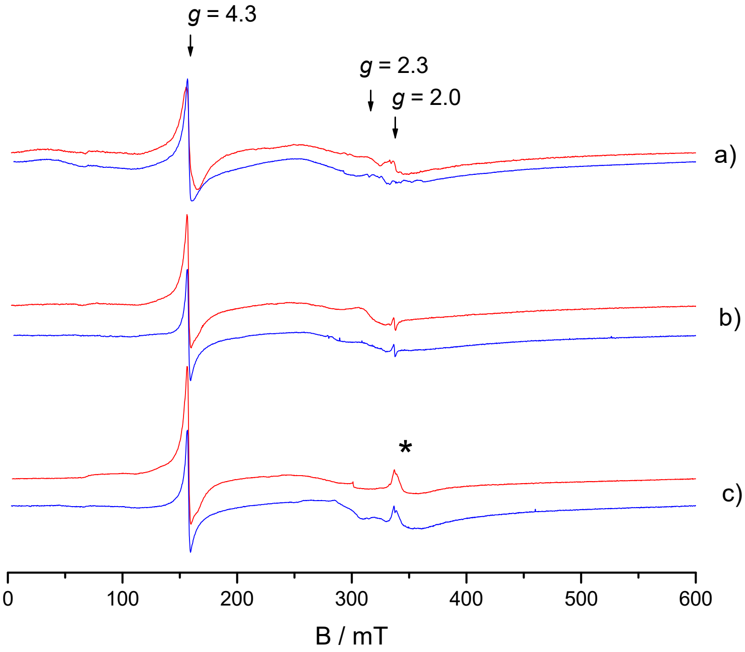

Figure 7. E. Shafia et al.

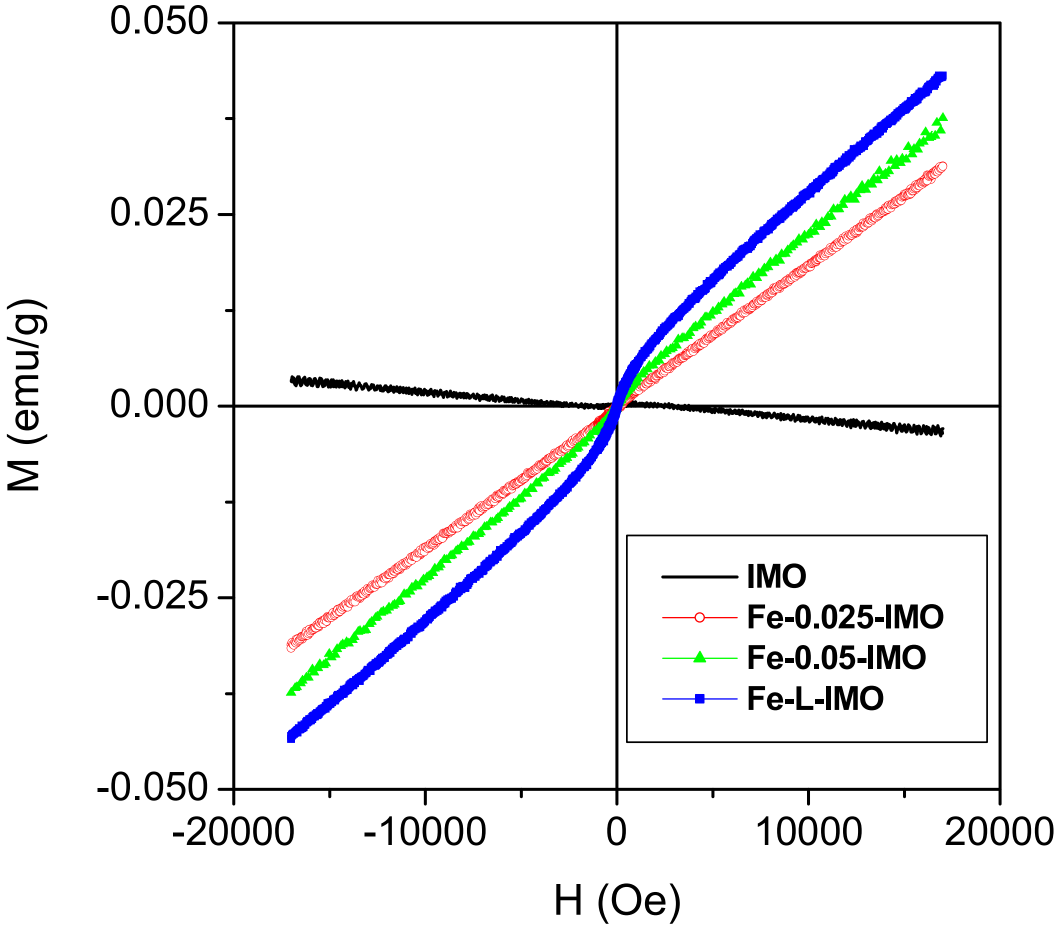

Figure 8. E. Shafia et al.

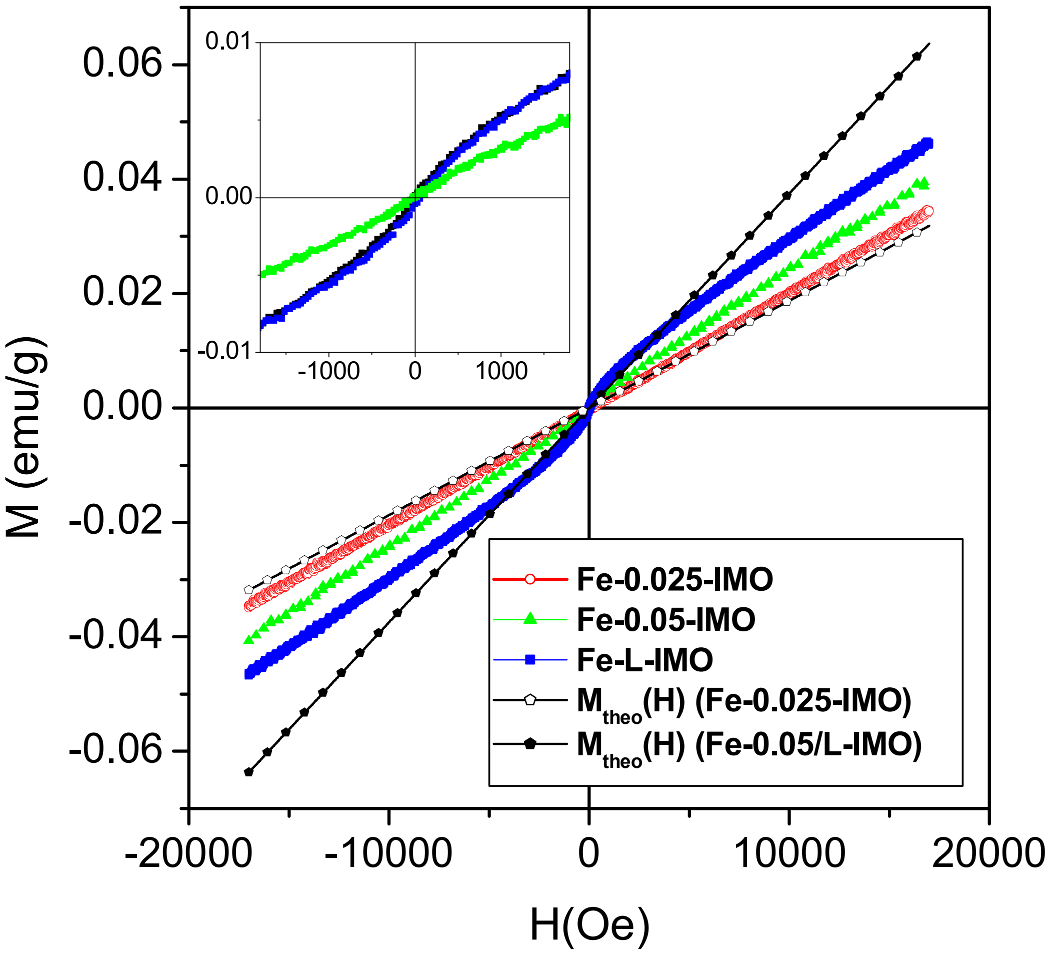

Figure 9. E. Shafia et al.

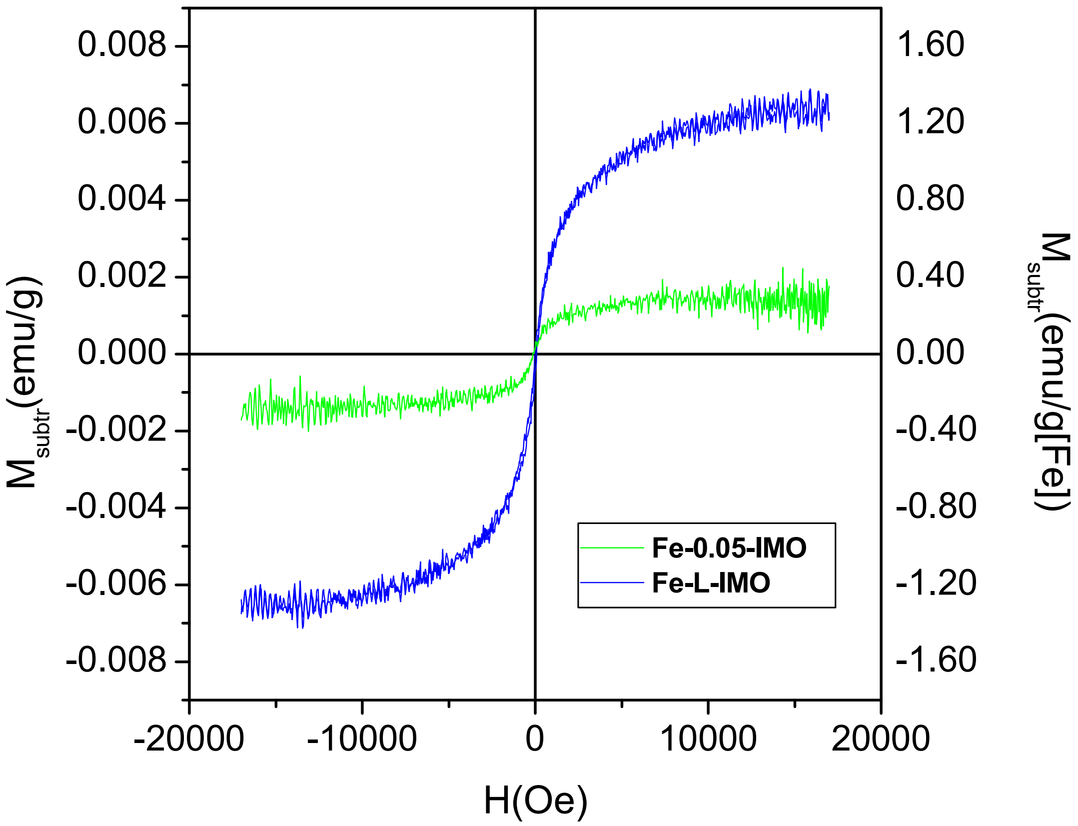

Figure 10. E. Shafia et al.

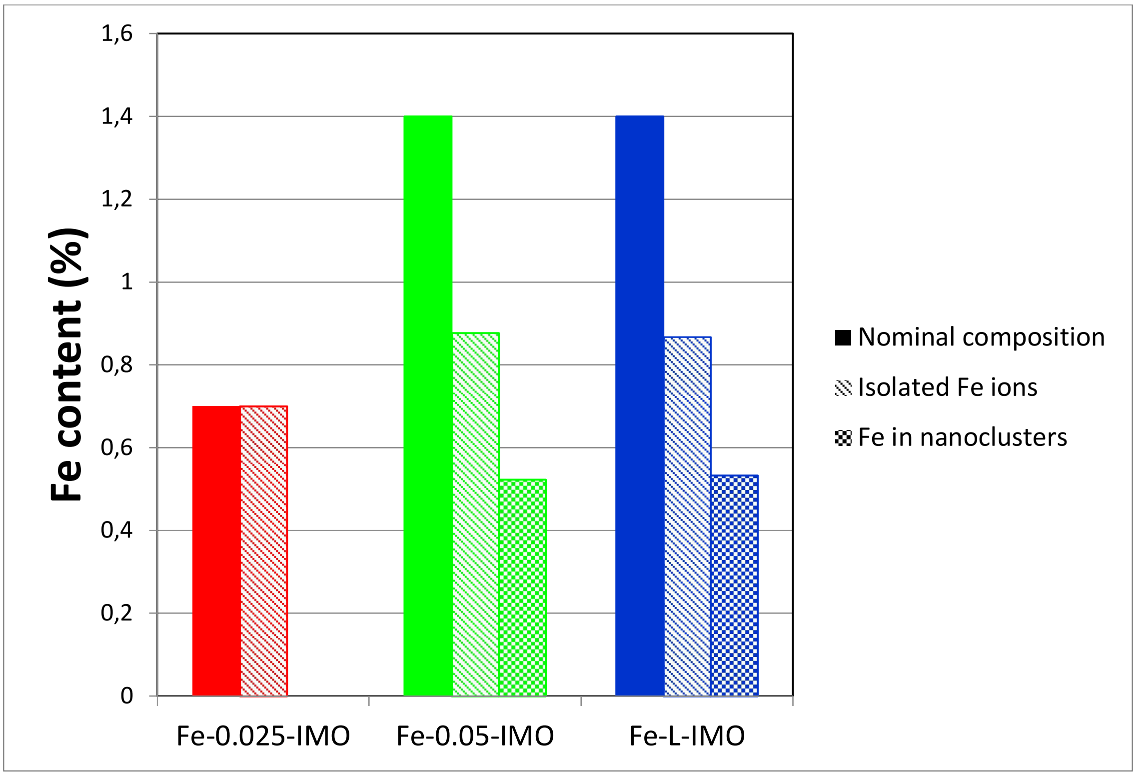

Figure 11. E. Shafia et al.